The Effect of Fast Solar Wind on Ion Distribution Downstream of Earth's Bow Shock

Florian Koller[1] , Savvas Raptis[2] , Manuela Temmer[1] , and Tomas Karlsson[3]
[1] Institute of Physics, University of Graz, Universitätsplatz 5, 8010 Graz, Austria; florian.koller@uni-graz.at
[2] The Johns Hopkins Applied Physics Laboratory, Laurel, MD, USA
[3] KTH, Royal Institute of Technology, Division of Space and Plasma Physics, Stockholm, Sweden

Abstract

The solar wind gets thermalized and compressed when crossing a planetary bow shock, forming the magnetosheath. The angle between the upstream magnetic field and the shock normal vector separates the quasi-parallel from the quasi-perpendicular magnetosheath, significantly influencing the physical conditions in these regions. A reliable classification between both magnetosheath regions is of utmost importance since different phenomena and physical processes take place on each. The complexity of this classification is increased due to the origin and variability of the solar wind. Using measurements from the Time History of Events and Macroscale Interactions during Substorms mission and OMNI data between 2008 and 2023, we demonstrate the importance of magnetosheath classification across various solar wind plasma origins. We focus on investigating the ion energy fluxes in the high-energy range for each solar wind type, which typically serves as an indicator for foreshock activity and thus separating the quasi-parallel from quasi-perpendicular magnetosheath. Dividing the data set into different regimes reveals that fast solar wind plasma originating from coronal holes causes exceptionally high-energy ion fluxes even in the quasi-perpendicular environment. This stands in stark contrast to all other solar wind types, highlighting that magnetosheath classification is inherently biased if not all types of solar wind are considered in the classification. Combining knowledge of solar wind origins and structures with shock and magnetosheath research thus contributes to an improved magnetosheath characterization. This is particularly valuable in big-data machine-learning applications within heliophysics, which requires clean and verified data sets for optimal performance.

Unified Astronomy Thesaurus concepts: Planetary bow shocks (1246); Space plasmas (1544); Heliosphere (711); Fast solar wind (1872); Solar coronal holes (1484); Solar wind (1534); Plasma astrophysics (1261); Plasma physics (2089); Solar-terrestrial interactions (1473); Interplanetary medium (825); Shocks (2086); Space weather (2037)

1. Introduction

The solar wind plasma gets shocked as it encounters the magnetic field of the Earth, forming the bow shock and the downstream magnetosheath region. The interplanetary magnetic field (IMF), which is convected with the solar wind, determines the behavior of the plasma surrounding the shock. The IMF angle at the shock surface θ_{Bn} divides the shock into a quasi-parallel ($\theta_{Bn} < 45°$) and quasi-perpendicular ($\theta_{Bn} > 45°$) region. The behavior of the magnetosheath exhibits notable distinctions behind the quasi-parallel and quasi-perpendicular shock. The quasi-parallel plasma region is strongly affected by the foreshock upstream of the shock, which is characterized by a mixture of incoming and backstreaming plasma and induces waves, decelerates solar wind, and forms nonlinear structures (Eastwood et al. 2005). Due to the presence of the foreshock, the downstream region displays a heightened energy flux as well as increased magnetic field variations. The quasi-perpendicular shock shows an increase in temperature anisotropy while lacking high ion energy fluxes. The subsequent impact on Earth's magnetic field and geoeffectiveness is fundamentally different in both regions. Figure 1 shows an overview of the dayside terrestrial magnetosheath.

Typical in situ classification of the magnetosheath relies on ion plasma moments. By measuring the energy flux one can infer the spacecraft's position in either the quasi-parallel or quasi-perpendicular magnetosheath (Raptis et al. 2020b). Karlsson et al. (2021) provide a framework for classifying magnetosheath based on Cluster (Escoubet et al. 1997) spacecraft observations using nine sample times between 2003 and 2009. They used cases with one spacecraft in the upstream solar wind and one in the downstream magnetosheath to confirm the angle Θ_{Bn}, restricting all measurements close to the shock. They used the integrated energy flux of the highest four energy bins of the Cluster Ion Spectrometer (CIS) Hot Ion analyzer (HIA) (Reme et al. 1997). Based on this data set, they defined thresholds to differentiate between quasi-parallel and quasi-perpendicular magnetosheath. They also differentiated the magnetosheath based on the magnetic field component standard deviation and ion temperature anisotropy.

While in situ properties can provide a classification as mentioned above, it should be noted that the upstream solar wind, which is responsible for the sheath formation, can also be classified into different types based on its origin on the Sun. The magnetosheath classification efforts discussed above have not taken different solar wind sources into account, which can significantly impact the results as we will show throughout this work. We follow the classification by Xu & Borovsky (2015) of four solar wind classes named after their origin: ejecta, coronal hole, sector reversal, and streamer belt. These categories can be associated to solar wind structures detected at Earth. Coronal mass ejections can be linked to ejecta, which usually describes low plasma beta, low Alfvén Mach number, high magnetic field strength with little fluctuation, and a non–
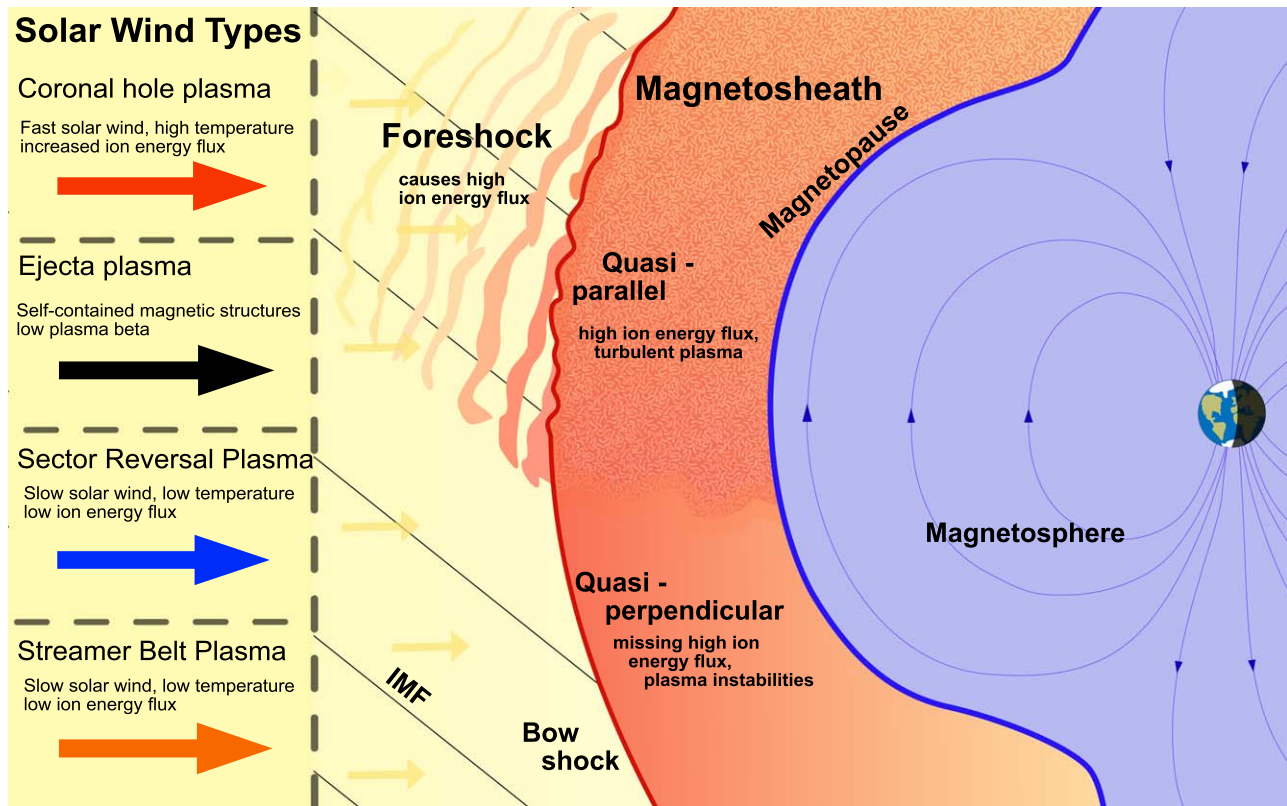
Figure 1. Schematic of the dayside magnetosphere and magnetosheath of the Earth. The system is affected by different incoming solar wind types (left side).

Parker spiral IMF angle. High-speed streams emanate from coronal holes (open magnetic field lines in the solar corona) and generate stream interaction regions when interacting with slow solar wind. This plasma is characterized by its high velocity, high temperature, and a low O^{7+}/O^{6+} ratio as well as an IMF orientation following the Parker spiral. The slow solar wind corresponds mainly to sector reversal or streamer belt plasma. Sector reversal plasma is associated with plasma coming from the top of helmet streamers (cusp-like magnetic loops in the solar corona) and has very low velocity, a high O^{7+}/O^{6+} ratio, high Alfvén Mach number, little fluctuations, and a non–Parker spiral IMF angle. Streamer belt plasma is connected to regions between coronal holes and helmet streamers or loop arcades between coronal holes of same polarities (Xu & Borovsky 2015) with low velocity, intermediate Alfvén velocity, intermediate Alfvén Mach number, and the IMF angle following the Parker spiral. The occurrence of each type of solar wind structure changes significantly throughout a solar cycle (e.g., Temmer 2021).

A reliable categorization of the magnetosheath environment holds significant importance for related investigations. The quasi-parallel magnetosheath frequently exhibits dynamic pressure enhancements (so-called "jets"; Plaschke et al. 2018). Studies analyzed the connection between the occurrence of jets and upstream solar wind conditions (Vuorinen et al. 2019; Raptis et al. 2020b; LaMoury et al. 2021), solar wind structures (Koller et al. 2022, 2023), and long-term influence by the solar cycle (Vuorinen et al. 2023). Sorting the plasma environment into quasi-parallel and quasi-perpendicular is crucial to analyze jet generation, evolution, and properties (e.g., Raptis et al. 2020a, 2020b). Upstream foreshock mesoscale transients present in the quasi-parallel magnetosheath can also strongly affect

Earth's environment (Zhang et al. 2022a). The quasi-perpendicular magnetosheath is prone to plasma mirror mode or ion cyclotron instabilities (Soucek et al. 2015) while the presence of current sheets and turbulence is also different between each region (Yordanova et al. 2020; Gurchumelia et al. 2022). Processes connected to the radial distance are influenced as well, i.e., magnetosheath plasma can charge exchange with neutral hydrogen of Earth's outer exosphere close to the magnetopause (Fahr et al. 2018). This is largely controlled by solar wind parameter (Sokół et al. 2023) and shows dependencies on IMF orientation as well (Starkey et al. 2022).

This study demonstrates that different solar wind classes have a statistical influence on magnetosheath classification, primarily due to differences in high ion energy fluxes among solar wind types. Fast solar wind correlates with high ion energies, making the downstream plasma classification challenging. We investigate these effects in order to initiate improvements for future magnetosheath separation algorithms. This work utilizes data from Time History of Events and Macroscale Interactions during Substorms (THEMIS; Angelopoulos 2008), which spans more than a full solar cycle. The abundance of THEMIS measurements (year 2008–now) enables a statistically robust connection between specific solar wind types and magnetosheath plasma, which is now made possible by the growing data set of subsolar magnetosheath measurements.

2. Data

Our study utilizes OMNI data (King & Papitashvili 2005) to classify the solar wind and THEMIS data from the terrestrial magnetosheath covering the period from the beginning of 2008 to the end of 2022. We specifically use the THEMIS

Electrostatic Analyzer (ESA; McFadden et al. 2008) and Fluxgate Magnetometer (Auster et al. 2008) instruments in our analysis. THEMIS spacecraft are required to be within a 30° cone around the Sun–Earth line to restrict to subsolar dayside regions. Intervals of magnetosheath times were automatically detected using the method by Plaschke et al. (2013): the plasma density is required to be 2 times denser than the OMNI solar wind density and the 10 keV ion energy flux needs to be lower than the 1 keV ion energy flux. Only magnetosheath intervals ⩾30 minutes were considered. As the study is based on broad statistics, we interpolated all measurements used in the statistical analysis to 1 minute resolution. In the following analysis, we connect the magnetosheath measurements to the associated solar wind class defined by OMNI measurements.

The highest ESA ion energy flux bins were used, similar to Karlsson et al. (2021). There are in total four energy bins with values around 10 keV or greater, with the lowest starting at 8.1 keV. The uppermost energy flux that provides valid measurements in ESA usually shows a maximum energy level of up to 24.4 keV. The highest two to four bins were integrated as follows:

$$F_{\text{high},N} = \sum_{i=1}^{N} F_i^* \Delta E_i, \tag{1}$$

with F_i being the differential energy flux at channel i (with $i = 1$ being the highest channel) and ΔE_i being the width of the energy bin i. The energy bin width follows the width of logarithmically spaced energy flux steps. Thus, $F_{\text{high},1}$ denotes the flux of the highest bin, $F_{\text{high},2}$ the integrated flux of the two highest bins, and so on. The Cluster CIS-HIA energy fluxes used in Karlsson et al. (2021) have a higher upper range in the ion energy spectrum. Therefore, a one-to-one comparison of the integrated flux measure using the highest four bins would not quantitatively yield similar results between both missions. The highest three bins from THEMIS ESA have similar energy ranges and widths as the highest two to four energy bins in Cluster CIS-HIA, which is the largest overlap of energy range in this work and the measure used in Karlsson et al. (2021).

Utilizing the classification scheme established by Xu & Borovsky (2015) with a temporal resolution of 1 hr, we apply the methodology proposed by Camporeale et al. (2017) for solar wind classification through machine learning. The solar wind is categorized into four distinct origins: ejecta, coronal hole, sector reversal, and streamer belt. By using the same training set and a Gaussian process supervised learning model as Camporeale et al. (2017), we classified the 1 hr OMNI data set up to 2023. This method provides a probability per hour for each of the four classes instead of unambiguously putting events into one category. This allows the usage of a confidence level for selecting classes as described below. It should be noted that our statistical results were cross-validated for the periods obtained up to 2017 in the original paper with full agreement. This suggests that the rest of the classification period (2017–2023) follows the expected trends discussed in Xu & Borovsky (2015).

To ensure statistical robustness, we require that the classification probability for a single solar wind class exceeds and maintains 0.4 (40%) for a consecutive duration of at least 3 hr. We exclude the first and last hour of each solar wind class instance to avoid significant mixing of different solar wind classes. OMNI measurements are time-shifted by 2.5 minutes
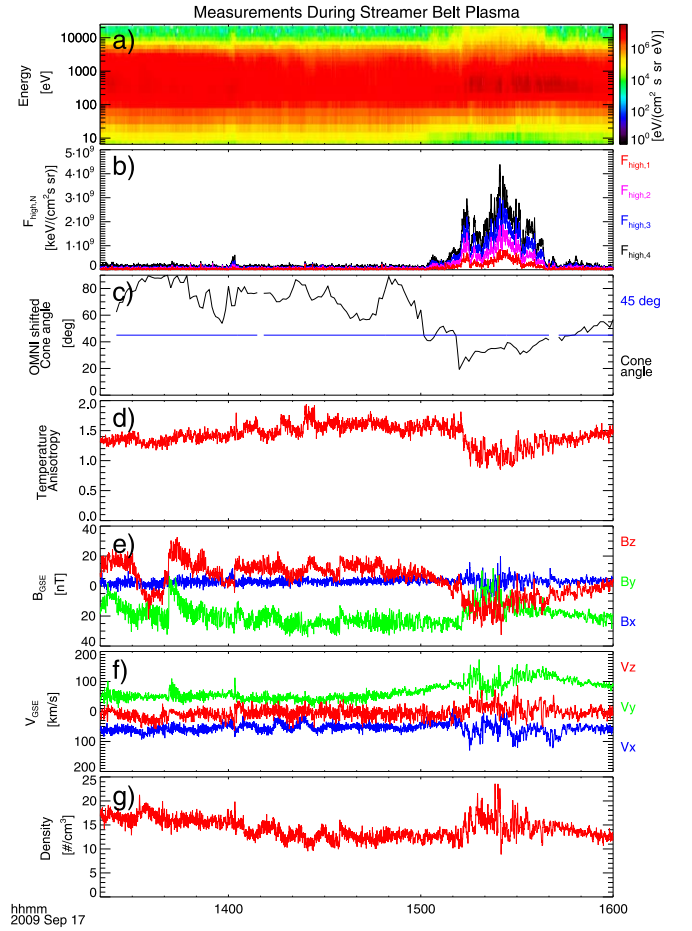

Figure 2. THEMIS A magnetosheath measurements during streamer belts origin plasma. The panels show (a) ion energy spectrum, (b) integrated top four bins of energy spectrum, (c) associated IMF cone angle, (d) temperature anisotropy, (e) magnetic field components, (f) ion velocity components, and (g) ion density.

with respect to THEMIS measurements to statistically account for the delay of the plasma moving from the bow shock nose to the spacecraft further down in the sheath. This amounts to a total usable data set of 3144.2 hr (52.4 days) divided into classes as follows: 1480.6 hr of sector reversal plasma, 891.3 hr of streamer belt plasma, 610.3 hr of coronal hole plasma, and 161.9 hr of ejecta plasma.

3. Results

The presence of high-energy ions can be used as an indicator that the spacecraft is downstream of the quasi-parallel shock. Figure 2 shows roughly 3 hr of magnetosheath measurements by THEMIS during a time when the solar wind plasma originated from streamer belts. Panel (a) shows the ion energy spectrum with a clear change in the behavior around 15:30, showing an energy increase in the highest channels. Panel (b) shows the integrated flux of these top four energy bins as defined by Equation (1). The increase correlates with the decrease of the OMNI IMF cone angle (panel (c)), indicating a switch of quasi-perpendicular to quasi-parallel plasma and back associated with the change in IMF direction. Both cone angle and simple thresholds on $F_{\text{high},N}$ could be effectively used to classify the magnetosheath in this event.

Figure 3 shows 4 hr of magnetosheath data during coronal hole plasma. The overall energy flux is increased: $F_{\text{high},4}$ is
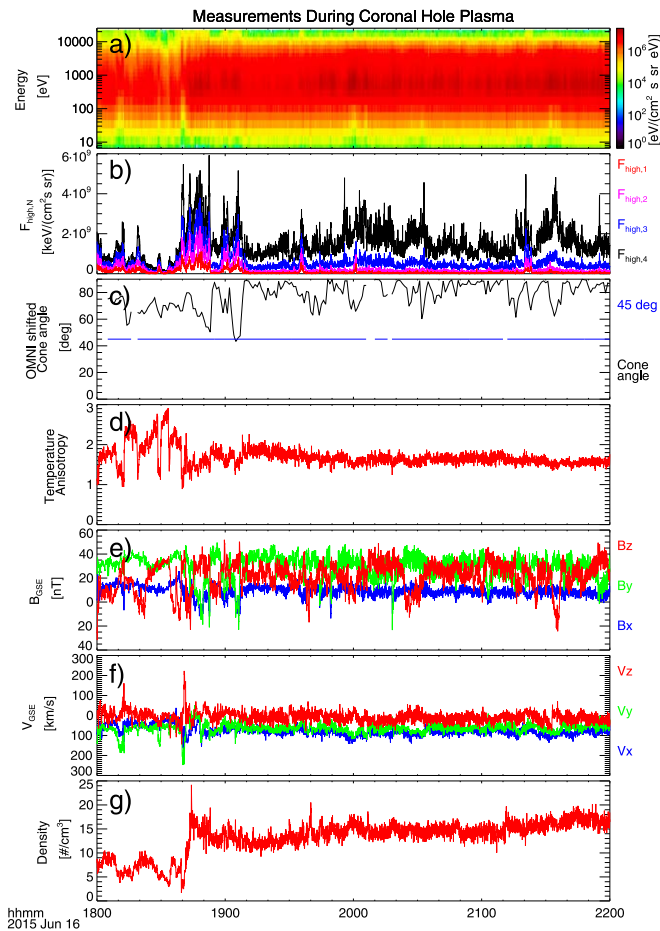
Figure 3. THEMIS A magnetosheath measurements during coronal hole origin plasma. The panels follow the same format as Figure 2.

heightened to a constant background level (black line in panel (b)). Quasi-parallel magnetosheath presence can be seen between 18:30 and 18:50, by the increase of ion flux in all higher-energy bins. This also coincides with decreasing cone angle values. However, the cone angle never falls below 45°, which makes its usage to classify the magnetosheath insufficient for this example. Using a threshold for $F_{high,3}$ or $F_{high,2}$ might work to classify the sheath, however, with little error margin compared to the clear increase visible in the streamer belt plasma example.

In order to separate the ion energy flux into high-energy regime (quasi-parallel) and low-energy regime (quasi-perpendicular), we analyze the statistical distribution of ion high-energy fluxes for each solar wind class. This corresponds to the total statistical distribution of the values shown in the examples of Figures 2(b) and 3(b). A double-peaked distribution is expected due to the difference in energy flux within the quasi-parallel and quasi-perpendicular region. Figure 4 depicts the high-energy histogram for solar wind classes for the top four integrated bins. Notably, the energy flux associated with coronal holes exceeds all other classes by a large margin in every panel. Sector reversal and streamer belt plasma show a double-peaked distribution in $F_{high,4}$, $F_{high,3}$, and less obvious in $F_{high,2}$. The broad distribution of coronal hole plasma in panel (a) peaks at values 2–7 times higher than the high-energy peak of other classes. The coronal hole plasma cannot be easily divided into subsections in any flux bins, only showing a slight

indication of a double-peaked distribution in panels (b) and (c). Ejecta plasma shows a prolonged distribution at higher-energy fluxes instead of a peak in all panels, suggesting mostly quasi-perpendicular plasma. The overlap between the distributions of coronal hole plasma and the other classes is the largest in $F_{high,1}$ (panel (d)). However, other solar wind types do not show a clear distinction between high- and low-energy flux regime using $F_{high,1}$.

Lastly, we use cone angle characterization to explore the quasi-parallel and quasi-perpendicular plasma energy flux distributions for each solar wind type. For this purpose, we divide the $F_{high,3}$ distribution (Figure 4(b)) into high ($>60°$), intermediate ($30° < \Phi < 60°$), and low cone angle ($<30°$) regimes. Figure 5 shows the $F_{high,3}$ energy flux histograms for each solar wind class for the aforementioned cone angle regimes. Panel (a) displays the $F_{high,3}$ distribution under high cone angles, corresponding to low-energy quasi-perpendicular magnetosheath plasma. Panel (b) represents the cone angle histograms associated with the values in panel (a). Notably, the energy flux of quasi-perpendicular plasma in coronal holes is roughly 1 order of magnitude higher than in all other classes. Moving to the $F_{high,3}$ energy flux in intermediate cone angle regimes, we see a distinct bimodial distribution in ejecta, sector reversal, and streamer belt plasma. This indicates a mix of quasi-parallel and quasi-perpendicular magnetosheath plasma. A gray line at $0.2 \times 10^9 \, \mathrm{keV \, cm^{-2} \, s^{-1} \, sr^{-1}}$ is included to highlight the dip position between both peaks, serving as an approximate separator for quasi-parallel and quasi-perpendicular magnetosheath. There is no bimodial $F_{high,3}$ distribution visible in coronal hole plasma in intermediate cone angle regimes. Panel (e) shows the $F_{high,3}$ distribution at low cone angles (corresponding to panel (f)), which should statistically represent high-energy quasi-parallel magnetosheath. As expected, the $F_{high,3}$ distributions for sector reversal, streamer belt, and ejecta plasma have peaks at higher-energy fluxes. The small peaks at lower energies in sector reversal and streamer belt plasma likely represent a residual quasi-perpendicular plasma population due to the cone angle not correctly representing the subsolar magnetosheath. Coronal hole origin plasma distribution at low cone angles gradually increases and peaks at values roughly 3–7 times higher than other solar wind types. The broad $F_{high,3}$ coronal hole plasma distribution in all regimes indicates either a wide range of energy flux for quasi-parallel and quasi-perpendicular plasma or a high percentage of incorrect cone angle characterization. Using information from panels (a), (c), and (e), a separator line (red) for coronal hole plasma was inserted at $1.6 \times 10^9 \, \mathrm{keV \, cm^{-2} \, s^{-1} \, sr^{-1}}$, approximately 8 times higher than the separator line for other classes. The gray separator line would categorize most instances of coronal hole plasma as quasi-parallel, independent of the cone angle.

4. Discussion and Conclusion

We demonstrated that magnetosheath plasma originating from coronal holes would be almost exclusively classified as quasi-parallel plasma when using an energy-flux-based threshold obtained on average solar wind conditions. Statistically, the average cone angle in coronal hole plasma is lower compared to other solar wind types (Borovsky et al. 2019; Koller et al. 2023), resulting in more times of quasi-parallel plasma in the dayside magnetosheath. Previous studies found more magnetosheath jets in solar wind high-speed streams (corresponding to coronal hole plasma), also indicating an increase in quasi-
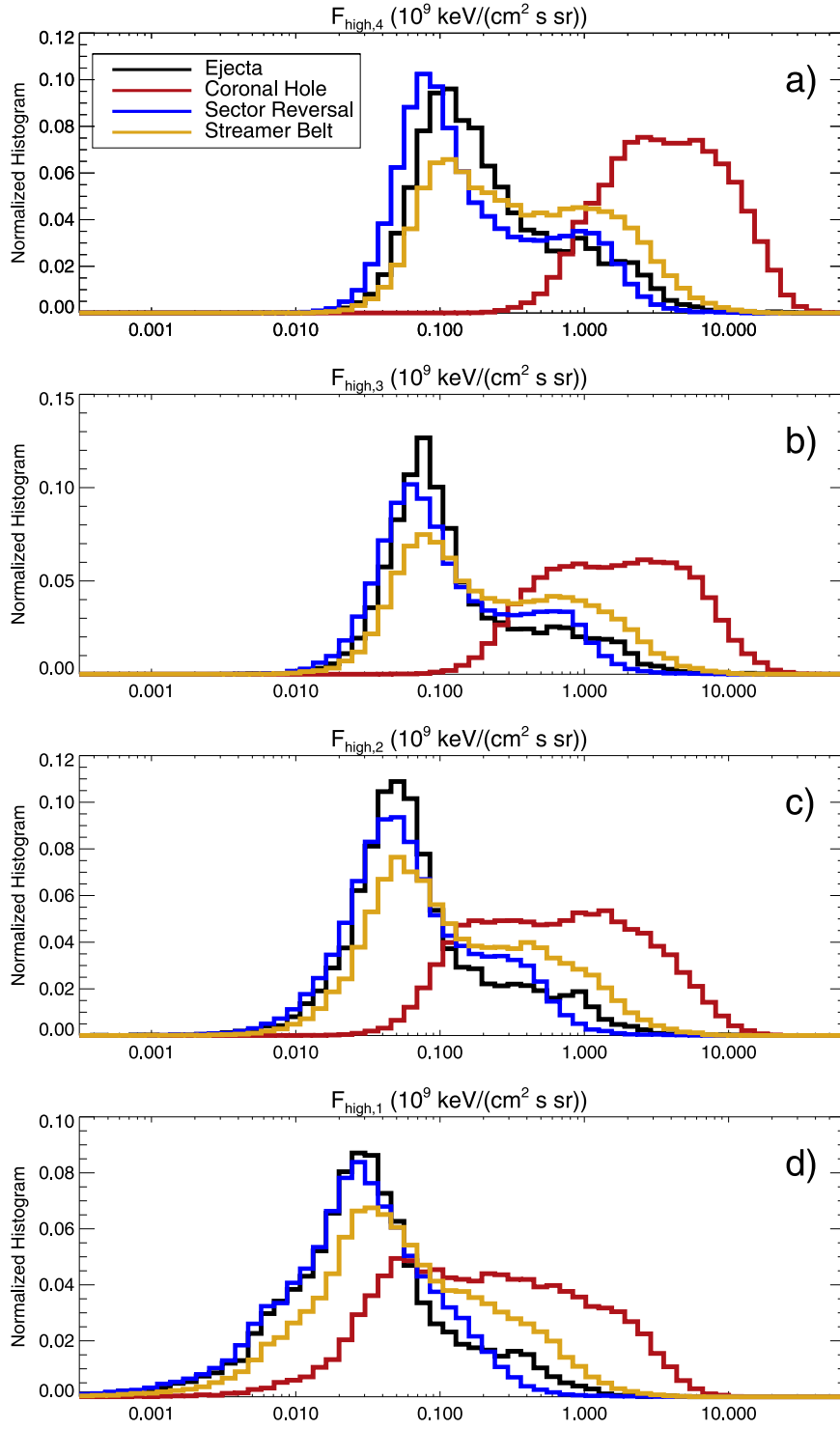
Figure 4. Normalized histograms of the highest four integrated energy flux bins given by Equation (1) for each solar wind type. Panel (a) corresponds to $F_{\text{high},4}$, (b) to $F_{\text{high},3}$, (c) to $F_{\text{high},2}$, and (d) to $F_{\text{high},1}$. The distribution of plasma originating in ejecta is given in black, coronal hole in red, sector reversal in blue, and streamer belt in orange.

parallel magnetosheath conditions (Koller et al. 2022, 2023). This could explain why classification biases might not have played an immediately visible impact in previous studies, as the increased time of quasi-parallel magnetosheath in coronal hole plasma has physical merit. However, it is unlikely that the magnetosheath environment in coronal hole plasma is in quasi-parallel condition all the time, as the cone angle distribution still peaks at values higher than 50° (Borovsky et al. 2019).

Our results indicate inherent problems when using the cone angle as a proxy for Θ_{Bn}. Even restricting the analysis to narrow angle regimes leaves residual populations of the opposite angle regime in most solar wind classes. There are several possible reasons for this mismatch. ACE and WIND spacecraft used to monitor upstream solar wind conditions are often far away from the Earth–Sun line (Borovsky 2018; Walsh et al. 2019). Solar wind structures smaller than this separation
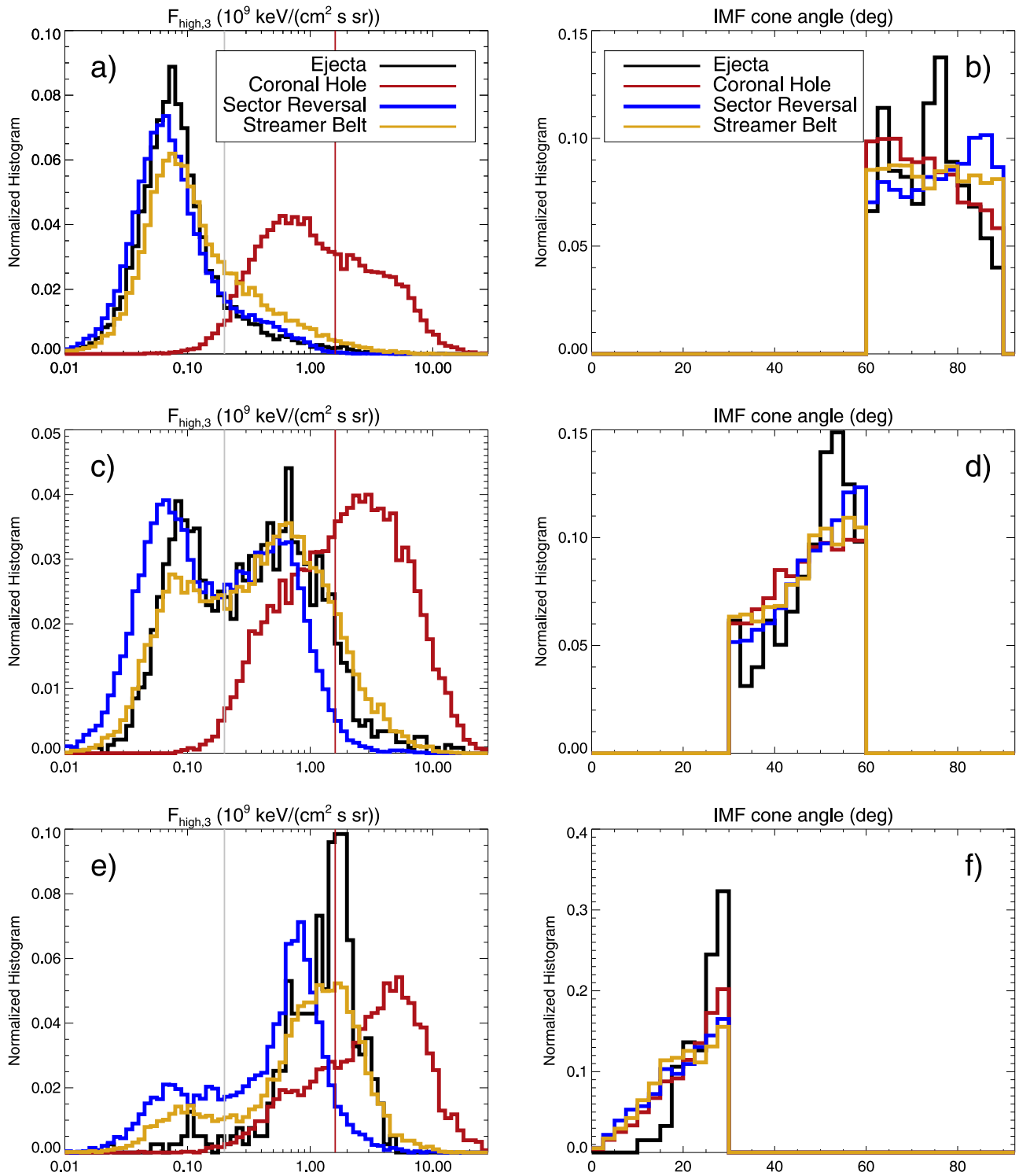
Figure 5. Normalized histograms of $F_{high,3}$ in different IMF cone angle regimes for each type of solar wind. Panels (a), (b), and (c) show the distribution given in Figure 4(b) divided into high, medium, and low cone angle conditions. Panel (b) shows the high cone angle distribution corresponding to panel (a), intermediate cone angles in panel (d) correspond to panel (c), and low cone angles in panel (f) correspond to panel (e). The same color code of Figure 4 is used.

can result in incorrectly propagated plasma properties to the bow shock. This uncertainty is further increased in coronal hole plasma, as it tends to show stronger magnetic field and velocity fluctuations compared to other types (Borovsky et al. 2019). Low cone angles also induce uncertainty into the prediction of values at the magnetosheath (Walsh et al. 2019). Using bow shock models can help to approach the actual Θ_{Bn} value, while

restricting to small solar zenith angles and positions close to the shock may also prove useful. Additionally, there might be a temporal offset due to the shifting of OMNI values from the bow shock nose to the actual spacecraft position in the magnetosheath. A way to mitigate propagation errors is to require stable IMF and magnetosheath conditions for the data set. However, this could rule out many events of explosive,

variable, and potentially geoeffective nature. Recent neural network efforts propagate L1 solar wind data to near-Earth space including uncertainty predictions, which could mitigate errors in future applications (e.g., O'Brien et al. 2023). Uncertainties due to mixing of different solar wind classes in coronal hole origin plasma is expected to be low, because this class has the highest likelihood of being correctly and unambiguously classified (Xu & Borovsky 2015; Camporeale et al. 2017). A different source of uncertainty is the reduction of energetic ions by processes in the magnetosheath, i.e., charge exchange with neutral, exospheric H-atoms close to the magnetopause (Fahr et al. 2018). Fuselier et al. (2020) reported that only 0.1% of the high-energy ions in the magnetosheath charge exchange; therefore we expect the statistical influence to be low.

Karlsson et al. (2021) also used the magnetic field standard deviation and plasma temperature anisotropy to differentiate quasi-parallel and quasi-perpendicular magnetosheath. These parameters should work reasonably well under ideal solar wind conditions close to the bow shock. However, they may also get affected by different solar wind classes and their properties. Strong magnetic field fluctuation often found in coronal hole plasma can persist even after crossing the bow shock: Figure 3 shows highly variable magnetic field components even within the supposedly quasi-perpendicular region. Temperature anisotropy is largely governed by the quasi-parallel and quasi-perpendicular shock. However, plasma expansion at the plasma depletion layer near the magnetopause can also cause large anisotropy values (Anderson & Fuselier 1993). As a result, the dependence of the temperature anisotropy on Θ_{Bn} is weaker close to the magnetopause (Soucek et al. 2015). Therefore, this parameter is also deemed to not be a reliable way to classify the whole magnetosheath.

Coronal hole origin plasma has a higher upper range in high-energy flux. While one can employ a threshold similar to Karlsson et al. (2021) at higher-energy levels, this might not hold for every event (see example cases in the Appendix). The usage of instruments with higher-energy levels might be beneficial for accurate classification. The THEMIS solid state telescope provides energetic ion fluxes $\geqslant 25$ keV. Two instruments on the Magnetospheric Multiscale mission (Burch et al. 2016) provide higher ion energy levels: the Energetic Ion Spectrometer of the Energetic Particle Detector (Mauk et al. 2016, $\geqslant 20$ keV), and the Fly's Eye Energetic Particle Spectrometer (Blake et al. 2016; $\geqslant 45$ keV). Automatic classifications of plasma environments using machine-learning techniques (like the work by Olshevsky et al. 2021, for solar wind, ion foreshock, magnetosheath, and magnetosphere) might improve classifications. To adequately train neural networks, one needs to be aware that coronal hole plasma data with reliable labels have to be consciously included in the data. Crucially, the occurrence of specific solar wind origin plasma changes drastically over a solar cycle. Coronal hole origin plasma, for example, dominates the decline phase of the solar cycle in the ecliptical plane (e.g., Temmer 2021). Machine-learning approaches exclusively trained during a specific solar cycle phase thus can have intrinsic biases and may provide unreliable results during other solar cycle phases.

In summary, this study provides results of high timeliness for currently ongoing studies related to characterizing and labeling of the magnetosheath using both conventional algorithms and machine-learning techniques, which is crucial for detailed analysis of the plasma downstream of collisionless shocks. Not considering the effect of different solar wind types may result in erroneous classifications. Supervised machine-learning techniques with training sets that lack specific solar wind class input may be inherently biased and unable to properly model the output when upstream conditions change. With the upcoming peak of the solar cycle, it is vital to build awareness of these issues. The interdisciplinary nature of our work connects solar wind and magnetospheric physics communities while providing key results for addressing the coupling between solar wind and planetary magnetospheres. Finally, using different types of solar wind input can be useful for remote sensing of the magnetosheath as a consequence of charge exchange processes. Energetic neutral atoms (ENAs) form due to the interaction of magnetosheath with neutral hydrogen close to the magnetopause (Fahr et al. 2018). ENA flux is mostly governed by solar wind dynamic pressure due to the compression of the magnetopause (Sokół et al. 2023). The high-energy ENA flux range is directly governed by magnetosheath ion flux (Fuselier et al. 2020) and is increasingly correlated with solar wind velocity at higher energies (Sokół et al. 2023). Different solar wind types thus are expected to largely affect ENA production, especially fast solar wind of coronal hole origin. Soft X-ray emission due to charge exchange processes also arises near the Earth's magnetopause (Sibeck et al. 2018). This emission can be affected by different heavy ion abundances in ejecta (Zhang et al. 2022b; Zhou et al. 2023), slow and fast solar wind (Whittaker & Sembay 2016). Different local soft X-ray emission in the quasi-parallel and quasi-perpendicular sheath might arise due to different thermal velocities in both regions (discussed in Sibeck et al. 2018) or by jets indenting the magnetopause (Yang et al. 2024). Solar wind upstream context and magnetosheath classification is thus highly relevant for observations, e.g., by the upcoming SMILE mission (Branduardi-Raymont & Wang 2022).

Appendix
Magnetosheath Examples in Different Solar Wind Origin Plasma

Here we show example events of magnetosheath plasma connected to each of the four solar wind types used throughout this work. This puts the statistical results shown in Figures 4 and 5 into the context of actual in situ measurements. The focus of the following examples lies on quasi-perpendicular plasma, sometimes intersected with quasi-parallel plasma as well. The left panels of Figure 6 show magnetosheath measurements
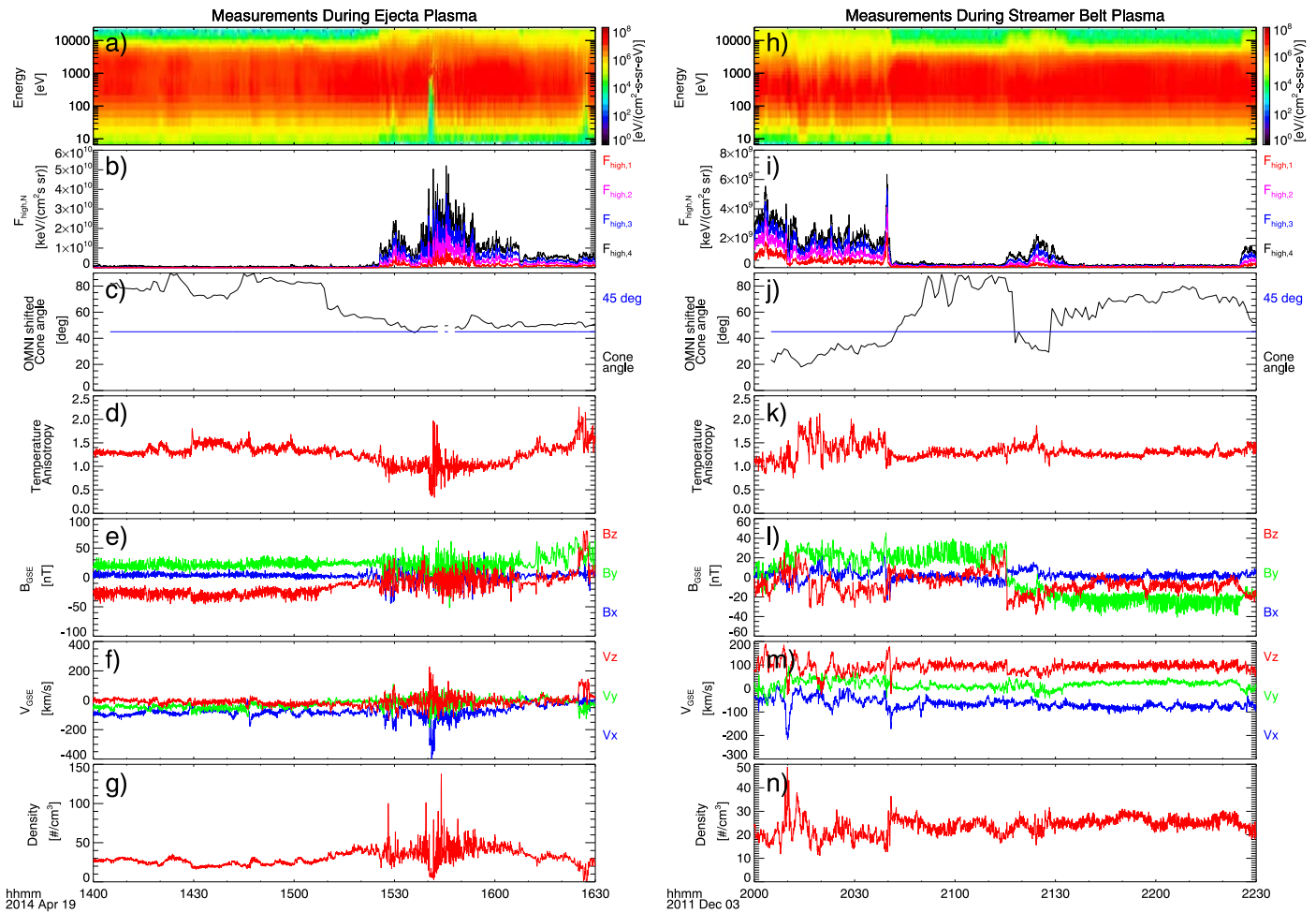
Figure 6. Example events of magnetosheath measurements by THEMIS A during ejecta (left) and streamer belt (right) plasma. The panels show ion energy spectrum (a), (h); integrated top four bins of the energy spectrum (b), (i); associated OMNI IMF cone angle (c), (j); temperature anisotropy (d), (k); magnetic field components (e), (l); ion velocity components (f), (m); and ion density (g), (n).

during plasma originating from solar ejecta. A clear interval of quasi-parallel plasma is visible starting at 15:27 UT, coinciding with an increase in $F_{\mathrm{high},N}$, a decrease in cone angle, temperature anisotropy around 1, and fluctuating magnetic field, velocity, and density values. There is a short time period of solar wind plasma visible at approximately 15:40 UT. The right panels of Figure 6 show magnetosheath measurements during streamer belt plasma. The cone angle and high-energy bins fluxes reliably indicate quasi-parallel magnetosheath plasma until 20:40 UT and between 21:15 and 21:35 UT. Unlike the example given in Figure 2, the temperature anisotropy and magnetic field fluctuations are not sufficient to detect the quasi-parallel sheath in this case.

Figure 7 (left panels) shows magnetosheath measurements at the start of a period of sector reversal plasma. Here, we see a time interval of quasi-parallel plasma around 01:20–02:20 UT, coinciding with a low IMF cone angle, decreased temperature anisotropy, and fluctuating magnetic field, velocity, and density parameters. The highest-energy bin, however, appears to almost show zero flux throughout the whole event. This is in stark contrast to the example event of coronal hole plasma in the magnetosheath (Figure 7, right panels). Here, the ion energy flux is increased to such high levels that the top

integrated three and four energy bins show a constant enhancement throughout the given time interval, independent of quasi-parallel or quasi-perpendicular plasma. There are short periods of quasi-parallel magnetosheath, indicated by decreases in cone angle, temperature anisotropy values around 1, and fluctuating plasma parameters. This example also illustrates the difference between coronal hole events: the high ion energy flux is several times higher over the whole period compared to the coronal hole event in Figure 3. Specifically, the lowest values of $F_{\mathrm{high},3}$ in this event are larger than the maximum values of $F_{\mathrm{high},3}$ in Figure 3. Because of these differences, we see the broad statistical distribution of integrated ion flux for coronal hole origin plasma in Figures 4 and 5. Therefore, an energy flux threshold to classify the magnetosheath tailored to one specific event might not be valid for another one, even within the same solar wind type. On the other hand, the plasma environment in the event in Figure 7 could be reliably classified using temperature anisotropy, cone angle, and the standard deviation of the magnetic field. All of these classifications would not work for the coronal hole event in Figure 3, showcasing that the information on high ion energy flux is an essential tool for the in situ classification.
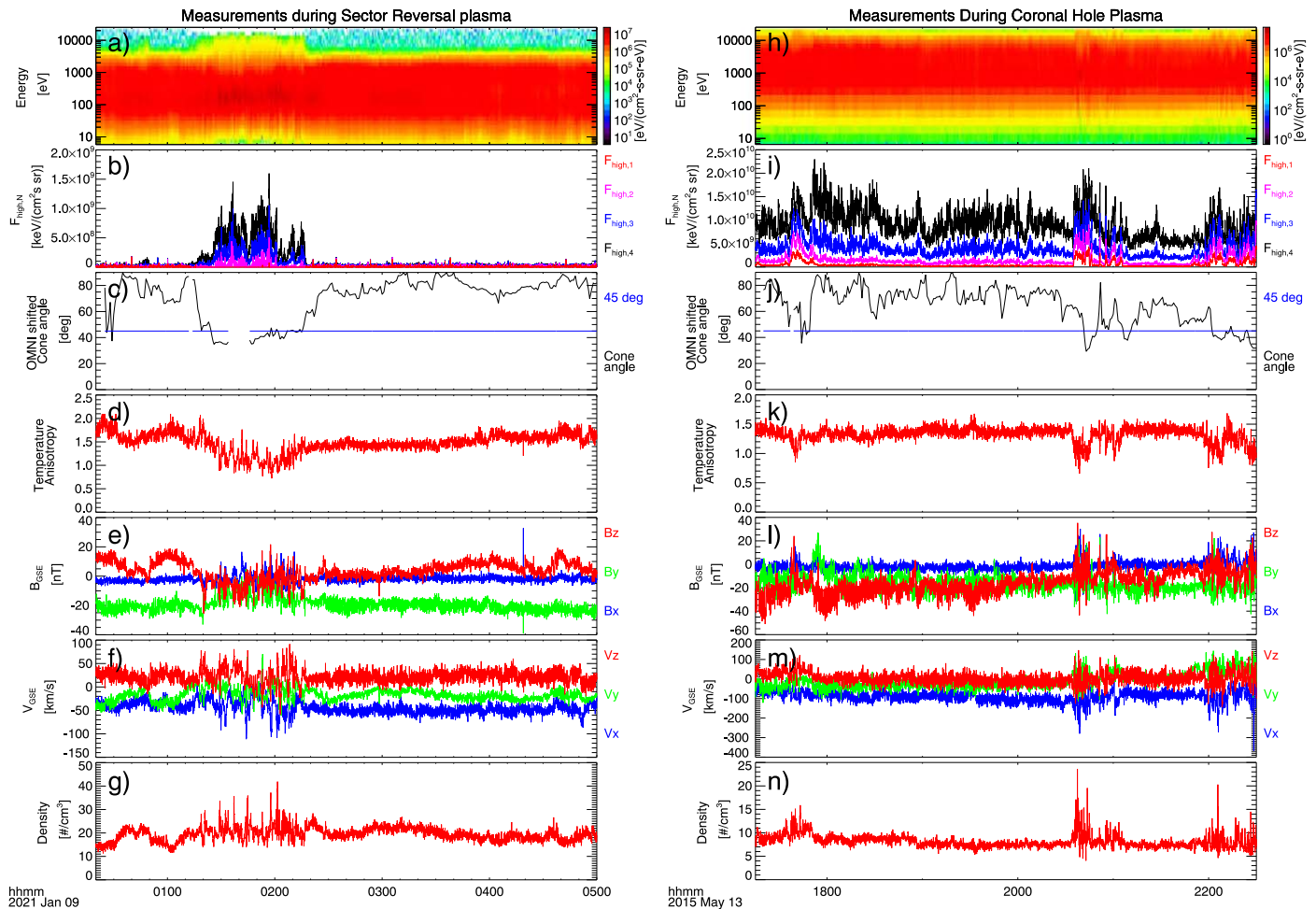
Figure 7. Example events of magnetosheath measurements by THEMIS A during sector reversal (left) and coronal hole (right) plasma. The panels follow the same structure as Figure 7.

ORCID iDs

Florian Koller ⬦ https://orcid.org/0000-0002-8164-0004
Savvas Raptis ⬦ https://orcid.org/0000-0002-4381-3197
Manuela Temmer ⬦ https://orcid.org/0000-0003-4867-7558
Tomas Karlsson ⬦ https://orcid.org/0000-0002-4546-5050

References

Anderson, B. J., & Fuselier, S. A. 1993, JGR, 98, 1461
Angelopoulos, V. 2008, SSRv, 141, 5
Auster, H. U., Glassmeier, K. H., Magnes, W., et al. 2008, SSRv, 141, 235
Blake, J., Mauk, B., Baker, D., et al. 2016, SSRv, 199, 309
Borovsky, J. E. 2018, JASTP, 177, 2
Borovsky, J. E., Denton, M. H., & Smith, C. W. 2019, JGRA, 124, 2406
Branduardi-Raymont, G., & Wang, C. 2022, in Handbook of X-ray and Gamma-ray
    Astrophysics, ed. C. Bambi & A. Santangelo (Singapore: Springer), 95
Burch, J. L., Moore, T. E., Torbert, R. B., & Giles, B. L. 2016, SSRv, 199, 5
Camporeale, E., Carè, A., & Borovsky, J. E. 2017, JGRA, 122, 10,910
Eastwood, J. P., Lucek, E. A., Mazelle, C., et al. 2005, SSRv, 118, 41
Escoubet, C. P., Schmidt, R., & Goldstein, M. L. 1997, SSRv, 79, 11
Fahr, H. J., Nass, U., Dutta-Roy, R., & Zoennchen, J. H. 2018, AnGeo, 36, 445
Fuselier, S. A., Dayeh, M. A., Galli, A., et al. 2020, GeoRL, 47, e89362
Gurchumelia, A., Sorriso-Valvo, L., Burgess, D., et al. 2022, FrP, 10, 903632
Karlsson, T., Raptis, S., Trollvik, H., & Nilsson, H. 2021, JGRA, 126,
    e2021JA029269
King, J. H., & Papitashvili, N. E. 2005, JGRA, 110, A02104
Koller, F., Plaschke, F., Temmer, M., et al. 2023, JGRA, 128, e2023JA031339
Koller, F., Temmer, M., Preisser, L., et al. 2022, JGRA, 127, e2021JA030124
LaMoury, A. T., Hietala, H., Plaschke, F., Vuorinen, L., & Eastwood, J. P.
    2021, JGRA, 126, e2021JA029592

Mauk, B., Blake, J., Baker, D., et al. 2016, SSRv, 199, 471
McFadden, J. P., Carlson, C. W., Larson, D., et al. 2008, SSRv, 141, 277
O'Brien, C., Walsh, B. M., Zou, Y., et al. 2023, FrASS, 10, 1250779
Olshevsky, V., Khotyaintsev, Y. V., Lalti, A., et al. 2021, JGRA, 126,
    e2021JA029620
Plaschke, F., Hietala, H., & Angelopoulos, V. 2013, AnGeo, 31, 1877
Plaschke, F., Hietala, H., Archer, M., et al. 2018, SSRv, 214, 81
Raptis, S., Aminalragia-Giamini, S., Karlsson, T., & Lindberg, M. 2020a,
    FrASS, 7, 24
Raptis, S., Karlsson, T., Plaschke, F., Kullen, A., & Lindqvist, P. 2020b,
    JGRA, 125, e2019JA027754
Reme, H., Bosqued, J. M., Sauvaud, J. A., et al. 1997, SSRv, 79, 303
Sibeck, D. G., Allen, R., Aryan, H., et al. 2018, SSRv, 214, 79
Sokół, J. M., Starkey, M. J., Dayeh, M. A., et al. 2023, JGRA, 128,
    e2023JA031669
Soucek, J., Escoubet, C. P., & Grison, B. 2015, JGRA, 120, 2838
Starkey, M. J., Dayeh, M. A., Fuselier, S. A., et al. 2022, JGRA, 127,
    e2022JA030965
Temmer, M. 2021, LRSP, 18, 4
Vuorinen, L., Hietala, H., & Plaschke, F. 2019, AnGeo, 37, 689
Vuorinen, L., LaMoury, A. T., Hietala, H., & Koller, F. 2023, JGRA, 128,
    e2023JA031493
Walsh, B. M., Bhakyapaibul, T., & Zou, Y. 2019, JGRA, 124, 3291
Whittaker, I. C., & Sembay, S. 2016, GeoRL, 43, 7328
Xu, F., & Borovsky, J. E. 2015, JGRA, 120, 70
Yang, Z., Jarvinen, R., Guo, X., et al. 2024, E&PP, 8, 59
Yordanova, E., Vörös, Z., Raptis, S., & Karlsson, T. 2020, FrASS, 7, 2
Zhang, H., Zong, Q., Connor, H., et al. 2022a, SSRv, 218, 40
Zhang, Y., Sun, T., Wang, C., et al. 2022b, ApJL, 932, L1
Zhou, Y., Yamasaki, N. Y., Toriumi, S., & Mitsuda, K. 2023, JGRA, 128,
    e2023JA032069